UNCONVENTIONAL RESOURCES TECHNOLOGY CONFERENCE
FUELED BY SPE • AAPG • SEG

URTeC: 2902457

High-Quality 3-D MicroCT Imaging of Source Rocks – Novel Methodology to Measure and Correct for X-Ray Scatter

Alexander Katsevich*[1-2], Michael Frenkel[1], Qiushi Sun[3], Shannon L. Eichmann[3], and Victor Prieto[1]

1. iTomography Corporation, Houston, Texas
2. Department of Mathematics, University of Central Florida, Orlando, Florida
3. Aramco Services Company: Aramco Research Center – Houston, Houston, Texas

Abstract

Micro Computed Tomography (microCT) of cores yields valuable information about rock and fluid properties at pore-scale for conventional rock and at rock heterogeneity scale for unconventionals. High levels of uncorrected X-ray scatter in CT data leads to strong image artifacts and erroneous Hounsfield Unit (HU) values making reconstructed images unsuitable for accurate digital rock characterization (e.g., segmentation, material decomposition, and others). MicroCT scanners typically do not include scatter correction techniques. To fill this gap, we developed a new methodology to measure and remove the scatter component from raw projection microCT data collected during rock core scans, and to ultimately improving image quality of scanned cores.

Widely used approaches for scatter estimation, based on Monte-Carlo simulation and simplified analytical models, are time-consuming and may lose accuracy when imaging complex unconventional shale cores. In this paper, we propose a more practical approach to perform scatter correction from direct scatter measurements, which is based on the Beam-Stop Array (BSA) method. The BSA method works as follows. The radiation scattered by the core sample is emitted in random directions. By placing an array of small, highly-absorbing beads between the source and the core, the primary X-ray signal through the beads is blocked, but the overall object scatter signal is not affected. The observed values in the beads' shadows on the detector are assumed to be scatter signal. Performing interpolation of the scatter signal between the observed pixels on the detector gives an estimate of the scatter signal at every pixel on the detector. Subtracting scatter from projection data yields corrected data used for 3D CT core image reconstruction.

To develop the core scatter correction methodology, we (1) performed modeling of primary and scatter signals to optimize the BSA design (beads layout, size, scan parameters); (2) developed and implemented an accurate scatter correction algorithm into our 3D microCT image reconstruction workflow, and (3) tested the proposed methodology using four shale core samples from the United States and the Middle East. To better assess the impact of scatter, all experiments with shale core plugs presented in this paper were conducted using a source energy of 160 kVp. Our results demonstrated that in many cases, especially with higher attenuating cores, scatter cannot be ignored due to its significant impact reducing accuracy of image reconstruction. We also showed that the developed methodology allows for accurate estimation and removal of scatter from the raw (projection) CT data, enabling reconstruction of high-quality core images required for performing digital rock analysis.

The presented scatter correction methodology is general and can be utilized with any microCT scanner employed by the petroleum industry to improve image quality and derive accurate HU values. This is of significant importance for quantitative characterization of highly-heterogeneous rock with fine structural changes as is the case for shale. Ultimately, this methodology should expand the operational envelope and value of microCT imaging in the Exploration & Production (E&P) workflows.

Introduction

X-ray Computed Tomography (CT), a common medical imaging modality, is based on measuring the attenuation of X-rays as the source and detector rotate around the patient (Townsend, 2010). Through sophisticated mathematical reconstruction, the set of attenuation maps collected for each source position (collection of radiographs in the raw data domain) is used to reconstruct a 3D grayscale image (volume in the image domain). X-ray attenuation at each energy level is directly related to the material density and the effective atomic number of the medium allowing for material identification. The grayscale value at each pixel is reported in Hounsfield Units (HU). In these units, the attenuations of water (μ_{water}) and air (μ_{air}) are equal to 0 HU and -1000 HU, respectively.

In the oil industry, medical X-ray CT is part of special core analysis, where variations in X-ray attenuation are used to identify mineral type, bulk density, porosity, fluid saturation, and other features for conventional cores (Wellington and Vinegar, 1987; Funk et al., 2011; Kwak et al., 2012). Medical X-ray CT, however, was designed to reconstruct features in larger objects (humans), and provides relatively low resolution (best voxel resolution 150 μm). Also, due to clinical regulations for patient safety, the maximum energy (low-100's kVp) for medical CT limits the range of materials that can be studied. This is particularly limiting for cores with highly attenuating materials such as pyrite.

For conventional, relatively homogeneous reservoir rock containing large pores or features, such as limestone and sandstone, medical CT provides accurate qualitative and quantitative analyses as shown in a number of publications over the last three decades (Vinegar, 1986; Wellington and Vinegar, 1987; Funk et al., 2011; Kwak et al., 2012; Siddiqui and Khamees, 2004; Coshell et al., 1994). Dual-energy medical CT studies are also described in the literature, where material decomposition for standards (Granton et al., 2008), carbonates (Siddiqui and Khamees, 2004; Al-Owihan et al., 2014), sandstones (Lopez et al, 2016), and shales (Walls and Armbruster, 2012; Almarzooq et al., 2014) are reported. The low-resolution and low maximum energy, however, limit the effectiveness of medical CT to provide quantitative analysis of reservoir rock with nano- and micron-scale textural variation and significant material heterogeneity such as is found in unconventional reservoir rock like shale.

Shale is comprised of various minerals and clays which are interlaced with organic matter (Passey et al., 2010), where the chemical composition, bulk density (ρ_b), and effective atomic number (Z_{eff}) varies for each component (Siddiqui and Khamees, 2004; Wenk and Bulakh, 2016). In addition to the organic and inorganic materials variation, air-filled and fluid-filled features, such as pores and fractures, may also be present and vary from one sample to the next. Variations in ρ_b and Z_{eff} are related to the X-ray attenuation coefficient μ for each component, and the difference in attenuation between adjacent components may be lower than the contrast resolution of medical CT. In this case, materials with different ρ_b and Z_{eff} will appear to be the same in the medical CT, which is undesirable for quantitative materials analyses.

Similarly, the nano- and micro-scale textural features of shale are well below the spatial resolution of medical CT. Microcomputed tomography (microCT) provides better spatial resolution (from ~1 μm to 10s of μm) and a wider energy range (maximum >200 kV) than medical CT. The higher resolution reduces the number of components that contribute to the attenuation for each voxel, and thus the data is more readily deconvolved to its constituents. In addition to compositional detection improvements, the higher resolution provides a more effective means to identify small-scale textural variations, lamination, and fractures, all of which are averaged in lower resolution measurements.

A higher maximum energy is also beneficial for shale analyses because the range of energies affects the range of materials that can be studied. When the scan energy is too low, the highly attenuating materials found in cores (i.e., pyrite, barite, and rutile) fully attenuate the beam, and image reconstruction becomes impossible. Alternatively, when the energy is too high, the least attenuating components (i.e., organic matter and air interfaces) attenuate too little, and there is little distinction between domains. Recent literature has demonstrated various applications of microCT for shales such as pore imaging, diffusion studies, and permeability assessment (Suhrer et al., 2010; Gelb et al., 2011; Tiwari et al., 2013; Fogden et al., 2014; Ly et al., 2017; Zhang et al., 2017).

Accurate correction for X-ray scatter is one of the most challenging problems in microCT imaging as the amount of scatter depends on scan geometry, X-ray source energy, core size, detector type, and other factors. MicroCT scanners use flat-panel detectors, which do not allow collimation (unlike curved detectors used in medical CT) and are not typically equipped with scatter correction, frequently leading to significant amount of scatter in the acquired raw CT

data. While the improved resolution and wider energy range are significant benefits of microCT, scatter correction is not a standard component of the reconstruction software, and reconstructed images may exhibit scatter-related artifacts.

Even though a significant fraction of scattered X-rays may reach the detector and contaminate the useful transmission signal, this effect is not accounted for by most reconstruction algorithms. Thus, scatter increases noise and reduces the signal-to-noise ratio (SNR) leading to artifacts in the reconstructed image (Sossin et al., 2016). Inaccuracies due to scatter are specifically problematic for applications where attenuation variations may be small, even though accurate reconstruction of these variations is critical for differentiating materials and accurate bulk density determination in shales. Increased error due to scatter can cause the detected attenuation in air-filled domains appear higher than expected and can lead to inaccuracies in the measured attenuation elsewhere. In turn, this reduces core image quality and impairs our ability to quantitatively measure density (both per voxel and bulk), distinguish materials with similar attenuation coefficients, and determine the effective atomic number. Common methods to estimate scatter, however, are indirect, relying on time-intensive Monte-Carlo (MC) simulations and simplified analytical models, which can be inaccurate.

Here we present a method to directly measure and correct for X-ray scatter in the microCT raw data domain based on the Beam-Stop Array (BSA) approach. The use of BSA-based X-ray scatter correction was reported in various applications, e.g., (Schörner, 2012; Sossin et al., 2016), and references therein. The use of the BSA-type methods in microCT core imaging workflows for Digital Rock (DR) applications relevant to the petroleum industry, however, appears to be novel.

In this study an internally designed, optimized, and fabricated BSA consisting of a PolyMethyl MethActylate (PMMA, also known as acrylic glass or Plexiglas) plate with embedded tungsten carbide beads is used to fully attenuate the primary X-ray beam at known locations on the detector. With the BSA positioned between the source and the sample, the measured signal in the shadows of the beads is a direct measure of scatter. In each experiment additional scans were collected using a second blank (without beads) PMMA plate of the same dimensions as the BSA plate to account for the effect of the PMMA medium.

The paper is organized as follows. First, we outline the scatter correction workflow and describe the MC-based simulations used to optimize the BSA design. The optimization step was completed with GEANT4 as the main computational engine for simulating scatter (Allison, et al., 2016; GEANT4, 2018) and includes BSA design optimization, measurement simulation, and the test-system for the proposed scatter correction algorithm. Then the data collection and algorithm validation methodology are described with additional implementation details. Next results are presented for shale core plug samples from North America and the Middle East. After the case study section, the practical impact and added value of the technology is presented followed by the conclusions of the study.

The results demonstrate a direct and highly accurate method to correct for X-ray scatter in microCT scans, which improves image quality and provides accurate quantitative imaging of cores. The latter is a requirement for more accurate DR applications, such as segmentation, multi-energy CT imaging for core material decomposition, and others.

Theory and Method

X-Ray Scatter Correction Method

The main concept behind the BSA-based method of scatter correction is as follows. Since the radiation scattered by the sample is emitted in random directions, scattered X-rays generally follow a ‘zig-zag’ path from the X-ray source to the detector. Therefore, a few small, highly-absorbing beads placed between the source and the scanned object (a core plug) will block the primary X-ray signal through the beads. Since the beads are small, the overall object scatter signal is not affected. The observed signal at the detector in the region directly behind the beads, the bead shadows, is, therefore, the scatter signal. X-ray scatter is a low spatial frequency signal, which varies slowly over the detector (Bootsma et al., 2013; Sisniega et al., 2013), so interpolating the scatter signal between the observed points (pixels) on the detector gives an estimate of the scatter signal at every pixel on the detector.

For this reason, the scatter correction algorithm requires the acquisition of two separate scans: one taken with the BSA in between the source and the core sample, and another – using the blank PMMA backing plate, without beam-stopping beads, located in the same place as the BSA. This ensures that the actual scatter observed in the scan with the blank plate is as similar as possible to the scatter observed behind the BSA beads.

For scatter analysis, let $D_{a,i}$ and $D_{b,i}$ denote the dark-current-corrected data at the i-th view of the blank plate and BSA (i.e., bead-containing) scans, respectively. Similarly, G_a and G_b denote the dark-current-corrected gain calibration (bright field) files of the blank plate and BSA scans, respectively. Note that the gain calibration files are collected with their respective plates as well. To compensate for scatter, we use the following formula

$$\hat{P}_i = \frac{D_{a,i} - \hat{D}_{b,i}}{G_a - \hat{G}_b} \tag{1}$$

where P_i denotes the estimated primary signal (transmittance rate), and $\hat{D}_{b,i}$ and $\hat{G}_b$ denote the interpolated data and gain images, respectively. The two latter images contain estimates for scatter at every point on the detector. Equation (1) is derived in the literature on scatter correction using BSA-based methods (e.g., Sossin et al., 2016).

Modeling of Primary and Scatter Signals to Optimize BSA Design

To determine the scatter simulation parameters and to have a baseline against which to compare the scatter correction algorithm, a model was used to simulate scatter and estimate the effectiveness of a BSA at measuring the scatter. For the purposes of obtaining high-quality scatter simulations, the open-source MC physics engine software GEANT4 (Allison et al., 2016; GEANT4, 2018) was used to simulate scatter in an experiment with similar geometry as the planned experimental scans. In this experiment, which did not include a BSA, a radiograph of a cylindrical shale core was generated, with the signal being separated into primary and scatter components. To approximate the material composition of a core, we used data provided by (Tenorio, 2016). The primary and scatter components (computed by GEANT4) were then used to model the primary and scatter components with different BSAs present. The following BSA parameters were changed: grid spacing, grid type (staggered or regular), and the bead diameter. Fig. 1 provides a schematic showing the parameters explored in BSA simulation. If P and S were the primary and scatter components computed by GEANT4, respectively, the following was used to estimate P_{BSA} and S_{BSA}:

$$P_{BSA} = xP, \quad S_{BSA} = (1-\alpha)S, \tag{2}$$

where x is the computed transmission of the BSA beads, and α is the proportion of total radiation to the core blocked by the BSA beads. Note that Equation (2) applies only to pixels in the shadows of the beads, which is all that is needed to apply Equation (1). To estimate what fraction of the beam is absorbed by the beads (denoted by x in Equation (2)), we simulated the X-ray beam spectrum using the program SpekCalc (Poludniowski et al., 2009), and used data from the National Institute of Standards and Technology (NIST) X-ray attenuation coefficient tables (NIST, 2018). It was found that 2 mm diameter tungsten-carbide beads attenuate 99.2% of photons emitted from an unfiltered 160 kVp X-ray source.

Accurate GEANT4 simulations are time consuming so a simplified approach for simulating a BSA was used. With our approach the scatter is simulated using GEANT4 once, and then the effect of the BSA design parameters is computed using the approximate formula in Equation (2). A quick validation of this setup was performed with a certain set of BSA parameters using GEANT4. The simulation and simplified model matched to a satisfactory degree. Note that the simulation does not include the effects of detector scatter. The effects of detector scatter are more challenging to determine and remain a topic of interest for future studies.

For each modeled BSA parameter set, the simulated primary and scatter data $P + S = D_a$ and $P_{BSA} + S_{BSA} = D_b$ (with and without BSA, respectively) were then used to generate simulated radiographs. For radiographs computed with differing BSA parameters, we generated estimates $\hat{P}$ for the true primary signal P using Equations (1) and (2) and the method laid out in the preceding paragraphs. The BSA was simulated to be placed at different vertical and horizontal coordinates to mimic inexact positioning. The average Root Mean Square (RMS) error of primary signal

estimation over several runs was taken to be the performance metric. Our simulations showed that the optimal beads arrangement is a staggered grid with a pitch of h = 8.5 mm between the beads in the horizontal and vertical directions.

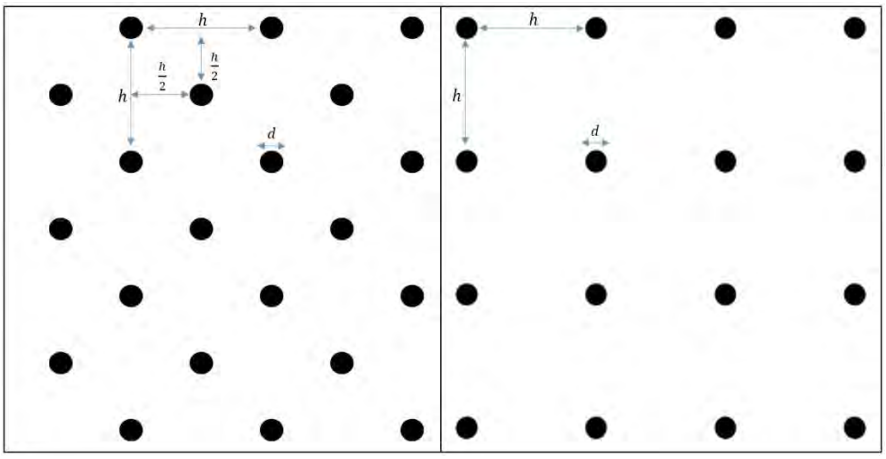

Figure 1: BSA Parameters. On the left is an example of a staggered grid; on the right is a regular grid. The BSA grids spacing is denoted by h, and the bead diameter is denoted by d.

Fabrication of BSA

A 4.5 mm-thick PMMA plate was cut to 50.8 mm (W) x 55.9 mm (H). The BSA contains fifty 2 mm diameter tungsten beads set in a 5 x 10 staggered grid. The center-to-center bead distance, h, in each row is 8.5 mm. Each row is separated by h/2 and the beads are offset by h/2 laterally (Fig. 2). The array of sink holes 3 mm deep were drilled using a 2 mm drill bit and a bead was placed in each hole, and then backed with foam to hold the bead in place. An additional blank plate (without beads) of the same dimensions was used in the BSA experiments.

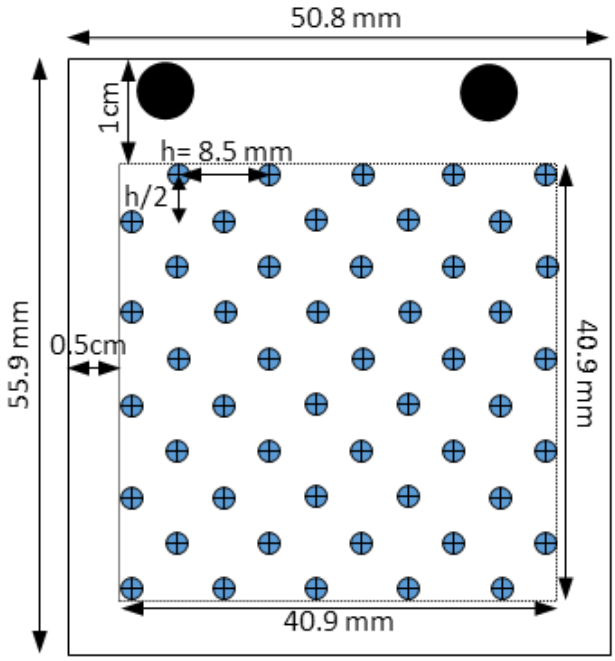

Figure 2: Specification of the fabricated BSA plate showing positions of the inserted tungsten beads (blue circles). An additional blank plate of the same dimensions was used in the BSA experiments.

Fig. 2 shows the BSA plate design, which was optimized using MC-simulations, and then fabricated for conducting BSA X-ray scatter measurement experiments with the selected four shale core samples.

Shale Core Samples Selected for the Study

Representative shale samples were selected solely based upon observable attenuation variations as well as other features within the core plug which are expected to contribute to scatter as they are directly relevant for this study. The four samples represent two North American shale and two Middle Eastern shale examples. Two Barnett Shale samples, Tarrant A-3 (6161.6 ft) and T.P. Sims #2 (7642 ft), were selected to represent North American organic rich shales. In the paper, we use nomenclature BEG-1 and BEG-2 for the samples Tarrant A-3 and T.P. Sims, respectively.

Two organic-rich shale samples from the Middle East, ME-1 and ME-2, were chosen for this study. Because the core sample ME-2 was fractured into two separate pieces, it was placed in a protective borosilicate glass case and affixed to ensure stability during X-ray scans. A full geologic and geochemical description of these samples is beyond the scope of this publication as this is included in other literature about the Barnett Shale (Zhang et al., 2012; Zhang et al., 2014) and Middle Eastern shale (Al-Sulami et al., 2017; Hakami et al., 2016) samples.

Scatter Measurement Experiments

Each core sample was scanned a total of three times, once for each of the three matters between the source and the core: (1) Air, (2) Blank PMMA plate, and (3) BSA plate. The first air scan is used for comparison between an uncorrected and scatter-corrected reconstructions. Only the second blank plate and third BSA scans are needed for scatter measurements and performing scatter-corrected reconstructions. The BSA and blank plates were placed at a fixed 70 mm distance from the X-ray source, using a mount made of the same as the blank and BSA plates PMMA material, in order to minimize additional scatter. All the experiments with shale core plugs presented in this paper were conducted using a source energy of 160 kVp (which is relevant for imaging shale cores) and a current of 125 μA.

The raw X-ray projection data was collected at the Aramco Research Center in Houston using a North Star Imaging (NSI) X5000 Industrial CT Scanner. Prior to this study, a repeatability survey had been performed on the scanner to ensure that the successive scans would be sufficiently similar for adequate comparison between scans and for scatter signal subtraction. The circular CT scans were performed with an angular resolution of 720 views per rotation. For the purposes of noise reduction, 8 frames were averaged per radiograph. The Source-Isocenter Distance (SID) and the Source-Detector Distance (SDD) were 100 mm and 1000 mm, respectively; providing the magnification factor of SDD/SID = 10. A voxel size of each reconstructed slice was 30 μm x 30 μm.

After all scans were performed, the raw projection CT data was transferred to a stand-alone GPU enabled computer to perform raw CT data processing, X-ray scatter estimation and correction, and image reconstruction using the iTomography software package.

Methodology for Scatter-Correction Algorithm - Validation and Implementation Details

The following section lays out details of the scatter correction algorithm along with our methods of comparison between reconstructions with scatter correction and without.

<u>First</u>, all four radiographs appearing in Equation (1): $D_{a,i}$, $D_{b,i}$, G_a, and G_b, were normalized to account for variations in source power. The BSA scans $D_{b,i}$ and G_b were then interpolated using a slightly smoothed thin-plate spline method. The normalization was done in pairwise fashion using edge pixels. This pair-wise normalization was applied successively in three following steps:

1. Data was normalized between the gain data of the blank PMMA plate and BSA scans G_a and G_b.
2. For each view of the scan, $D_{a,i}$ and $D_{b,i}$ were normalized against each other.
3. After estimating the scatter signal by interpolation, the pairs $D_{a,i} - D_{b,i}$ and $G_a - G_b$ were normalized against each other to ensure that the background value of their ratio is close to 1.0.

For uniformity, a similar normalization process was also applied to the air scan when performing reconstruction.

To investigate the effects of scatter correction, a reconstruction of the scan data collected without a plate (air scan) is compared to the scatter-corrected reconstruction. In both cases (air scan and scatter-corrected scan), the data were denoised in the radiograph domain. Because scatter correction reveals the true SNR, scatter-corrected data in some microCT scans were more heavily filtered than non-scatter corrected data.

Second, both reconstructions were independently corrected for beam-hardening using polynomial correction to remove cupping artifacts in a homogeneous region of the scan. The same Beam-Hardening Correction (BHC) parameter is used for the entire core image reconstruction workflow.

See Fig. 3 for an illustration of the BHC performance using, as an example, the core sample ME-2.

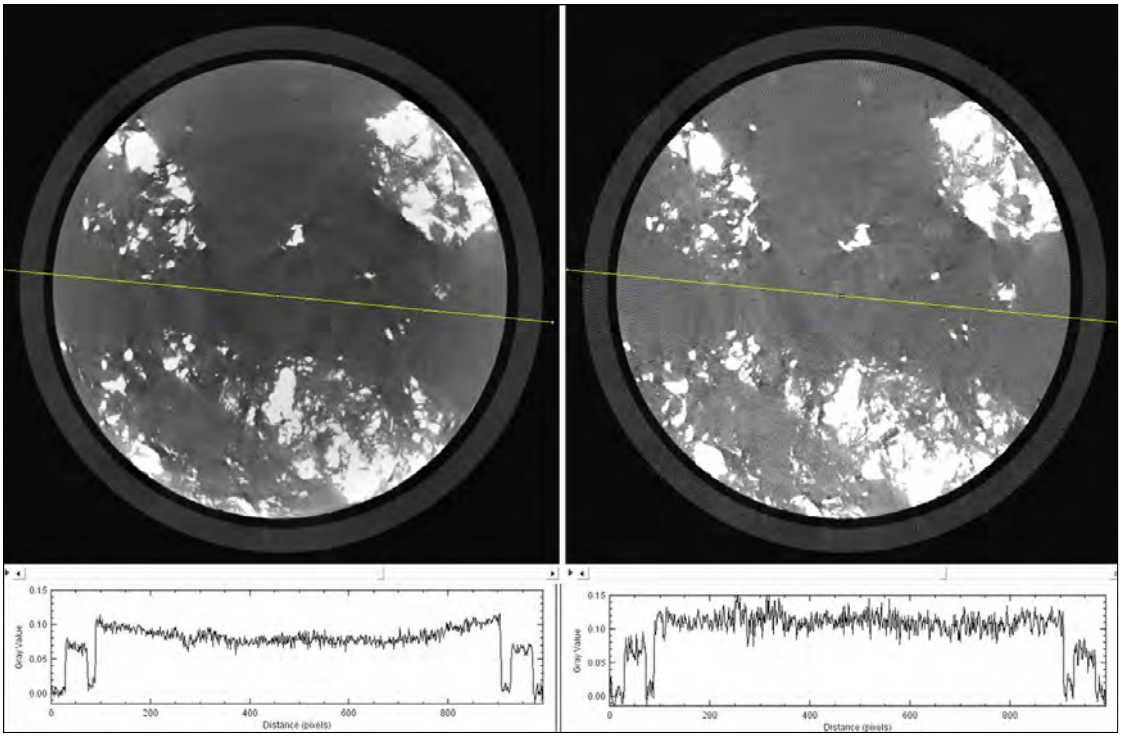

Figure 3: Illustration of the impact of BHC using the ME-2 core sample.
Left: A slice of the reconstructed core image computed without application of BHC.
Right: The same slice computed with application of BHC.
Line plots are taken along the yellow lines shown in both images.

The line profiles shown below the core images in Fig. 3, demonstrate that BHC was successfully applied to a relatively homogeneous region of the core. Note the lack of cupping artifacts on the right side, albeit with amplified noise due to application of BHC.

Results of Experiments with Core Sample ME-2

Scatter Correction Results

In this subsection we show the inner workings of the scatter estimation and correction process using the ME-2 core as an example. Fig. 4 shows the radiograph data (in log scale) that goes into the computation of the numerator in Equation (1). The data on the left and right correspond to the variables $D_{a,i}$ and $D_{b,i}$ in the equation, respectively. Note that $D_{b,i}$ has not been interpolated yet. We observe that the values in the blank plate data $D_{a,i}$ vary significantly within the core and drop down to about 2.4% of the background value. This is a fairly high attenuation for a 1-inch core plug, compared to the typical 17% transmission rate observed for samples ME-1 and BEG-1.

Additionally, we note that the shadows behind beads #1 and #6 have higher observed scatter than the shadows behind beads #3 and #4, which are located in the shadow of the most attenuating portion of the core. Another important observation is that the value observed behind bead #3, at about 1.9% of the background, is a substantial fraction of the 2.4% in the dark region. This is an indication that scatter forms a great proportion of the total signal in this dark region.

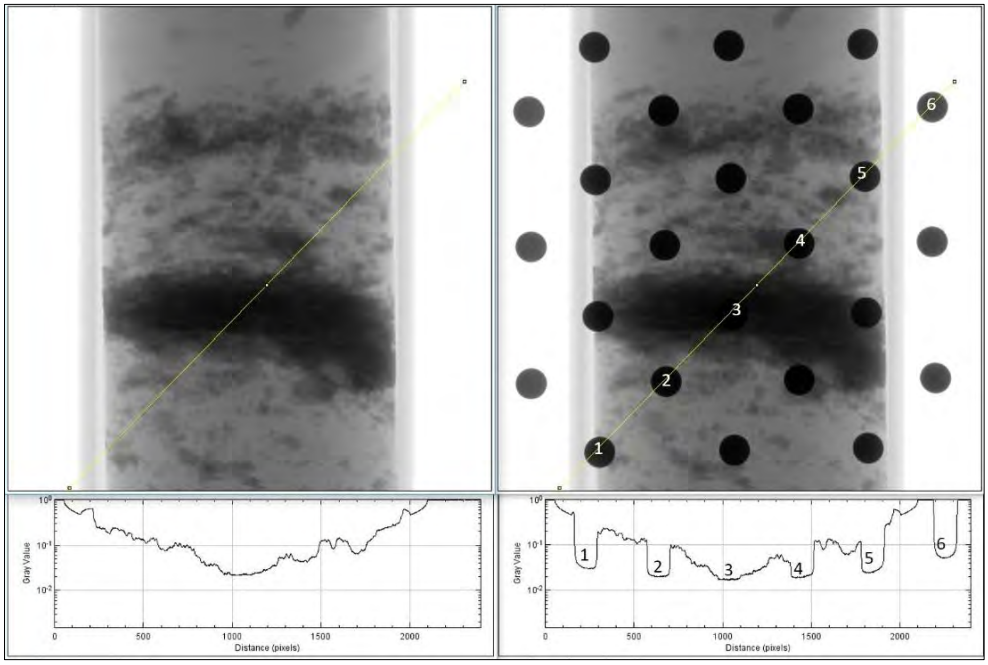

Figure 4: Illustration of Scatter Correction in Raw CT Data Domain – Example Input Images.
Left: Radiograph taken without using BSA ($D_{a,i}$). Right: The same source position radiograph taken with the use of BSA ($D_{b,i}$).
Both radiographs have been normalized for gain and corrected for dark current (offset) and are shown in log scale.
Line plots shown at the bottom are taken along the yellow lines in the radiographs
Bead numbers 1-6 along the yellow profile correspond to the numbers along the plot at the bottom.

Fig. 5 displays the interpolated values of $D_{b,i}$, $D_{b,i}$. This estimation of the scatter signal is subtracted from the observed signal with the PMMA plate $D_{a,i}$. We can see that the values of the interpolated scatter signal $D_{b,i}$ shown in the plot of Fig. 5 (center) at points labeled 1-6 do indeed correspond to the values observed inside of the BSA elements in Fig 4.

Additionally displayed in Fig. 5 is the ratio of the scatter estimate-to-total. From the profile plot in Fig. 5, we see that the observed value behind the beads in the dark region is about 80% of the signal measured. This indicates that scatter correction will produce significant difference in reconstructed values in this region.

Fig. 6 illustrates the effect that scatter correction has on the radiograph. For a fair comparison, a scan of the core taken with only air between the core and the source is compared to the scatter-corrected scan. We can see that in the scatter-corrected radiograph the estimated transmission in the highly-attenuating region has dropped from about 2% to 0.5%. This difference is about a factor of 4. In the log-scaled plots, the difference between the radiographs in lower-attenuation regions is not as noticeable.

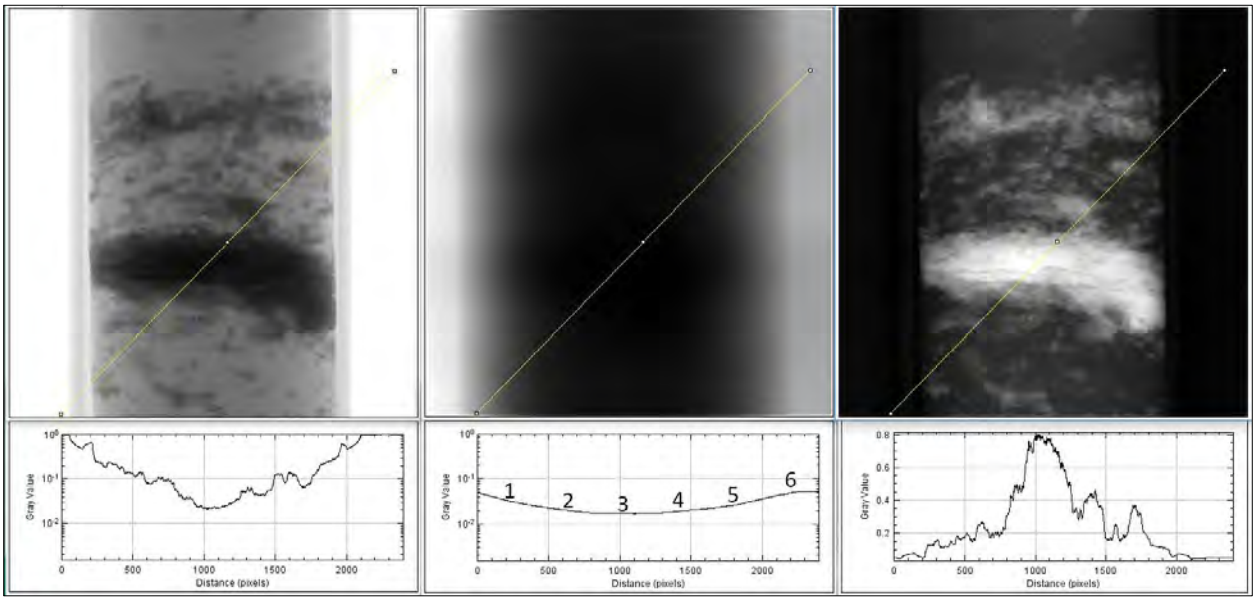

Figure 5: Scatter Correction in Data Domain – Scatter Estimation. From left to right:
Left: Original radiograph ($D_{a,i}$), Middle: Scatter estimate obtained by interpolating values in the shadow of the beads ($\hat{D}_{b,i}$),
Right: estimated scatter-to-total ratio ($\hat{D}_{b,i} / D_{a,i}$). Line plots are taken along yellow lines in the images.
The radiographs have been normalized for gain G_a and corrected for dark current (offset). Two left images are in log scale.

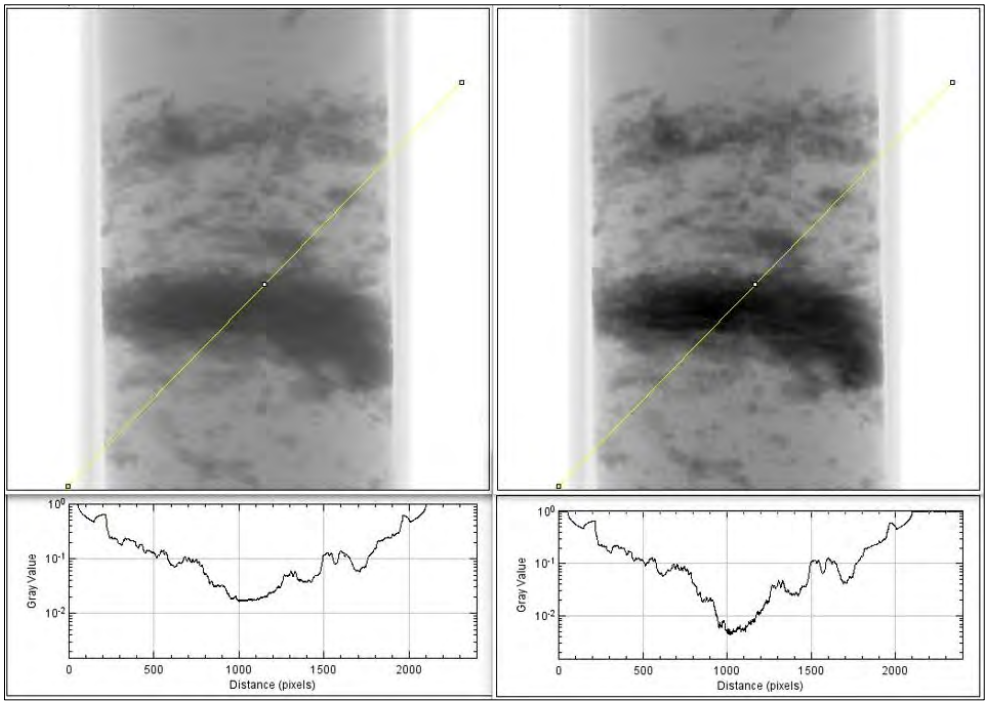

Figure 6: Scatter Correction in Data Domain – Comparison of Corrected and Traditional Scans.
Left: Traditional uncorrected scan radiograph, Right: Scatter-Corrected radiograph $\hat{P}$ (output of Equation (1)).
The radiographs have been normalized for gain, and corrected for dark current (offset) and are shown in log scale.
Line plots are taken along yellow lines in the images. Note the difference in values in the highly attenuating region.

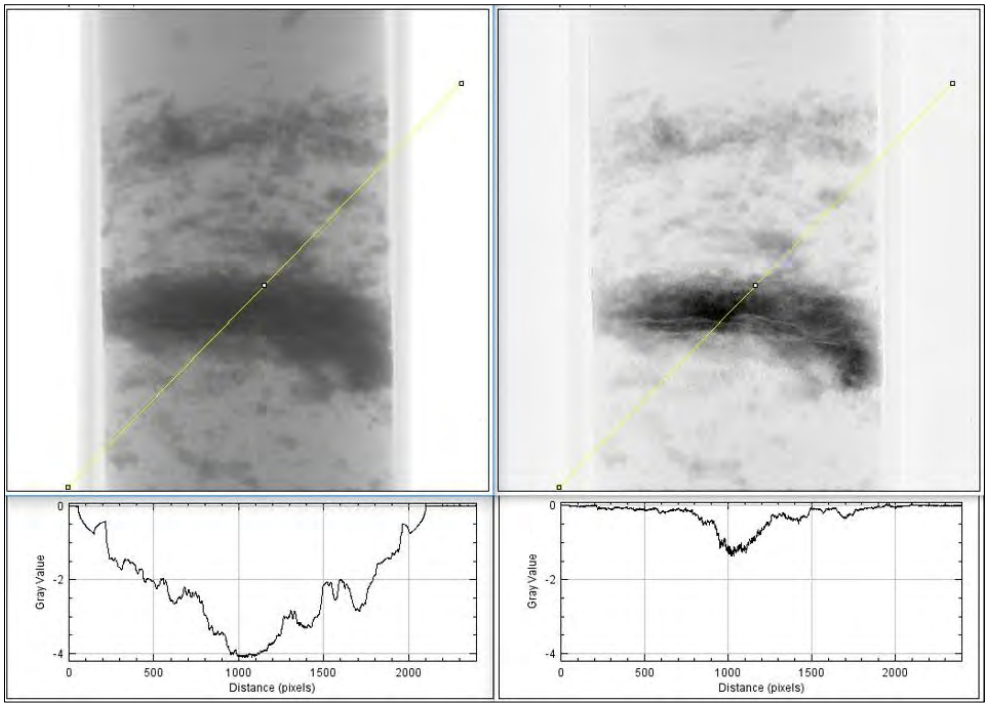

Figure 7: Scatter Correction in Data Domain – Impact of Correction. Left: Normalized radiograph (log scale) of uncorrected (air) scan. Right: Difference of logs – corrected and uncorrected (air) scans. Line plots are taken along yellow lines in the images. The images have been normalized for gain, and corrected for dark current (offset).

Fig. 7 displays the effects of scatter correction in more detail. The left plot in Fig. 7 shows the normalized air radiograph in the log scale. The right plot of Fig. 7 shows the difference between the logs of scatter-corrected (output of Equation (1)) and air radiographs. We are showing the difference of logarithms of the two radiographs, because the data in the log domain constitutes the input into the reconstruction algorithm. We can see from the profile plots of Fig. 7 that the value in the highly attenuating region did indeed drop (in the log domain) by close to about 1.3. This represents an increase in the input to the CT image reconstruction algorithm of about 32%.

Core Reconstruction Results

This section addresses the reconstruction-based results of the scatter-correcting algorithm. All four cores scanned are included in this section, with relevant results highlighted. As discussed in the sub-section *"Methodology for Algorithm Validation and Implementation Details"*, all reconstructions displayed are corrected for beam-hardening. Profile plots are displayed over key slices of the reconstructions. To more accurately display numerical differences between different reconstructions, key regions are highlighted and the mean reconstructed value in the region is present in the caption. We start with images comparing the original (i.e., not corrected for scatter) and scatter-corrected reconstructions of the ME-2 core.

Fig. 8 shows a sample cross-section of reconstruction in a homogeneous region of the ME-2 core. The flat profile plots show that beam-hardening correction (BHC) has been successfully applied to both the scatter-corrected and traditional reconstructions. In this region of the core, there seems to be little visual difference between the reconstructions.

Fig. 9 shows how some artifacts introduced by scatter were reduced by scatter-correction. We see that in the traditional air reconstruction, dark streaking artifacts appear in close proximity to highly-attenuating regions. The scatter-corrected scan shows great reductions in these streaks, which in some cases extend beyond the core to the glass encasing it.

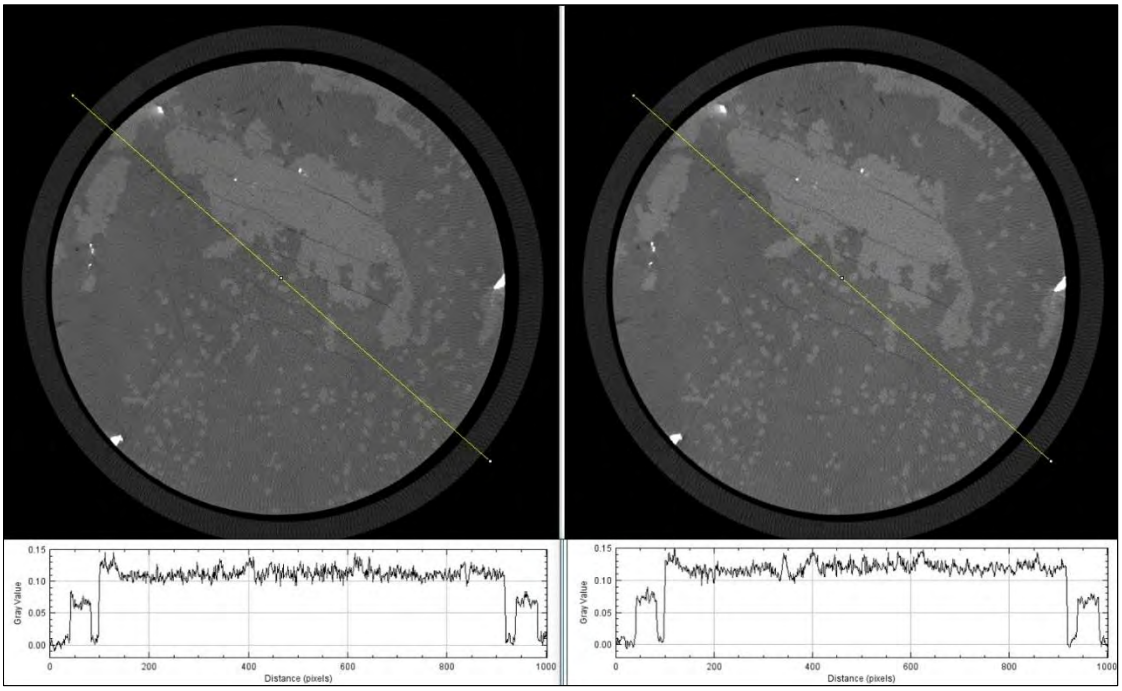

Figure 8: Cross-Section of Reconstruction for ME-2 Core.
This cross-section illustrates the region, which was used to determine the optimal BHC parameter.
Left – without scatter correction, Right – with scatter correction. Line plots are taken along the yellow lines in the images.
The plots demonstrate that BHC was successfully applied to a relatively homogeneous region of the core.
Note: The outer circle around the core is borosilicate glass, which encases the two-piece core for added stability.

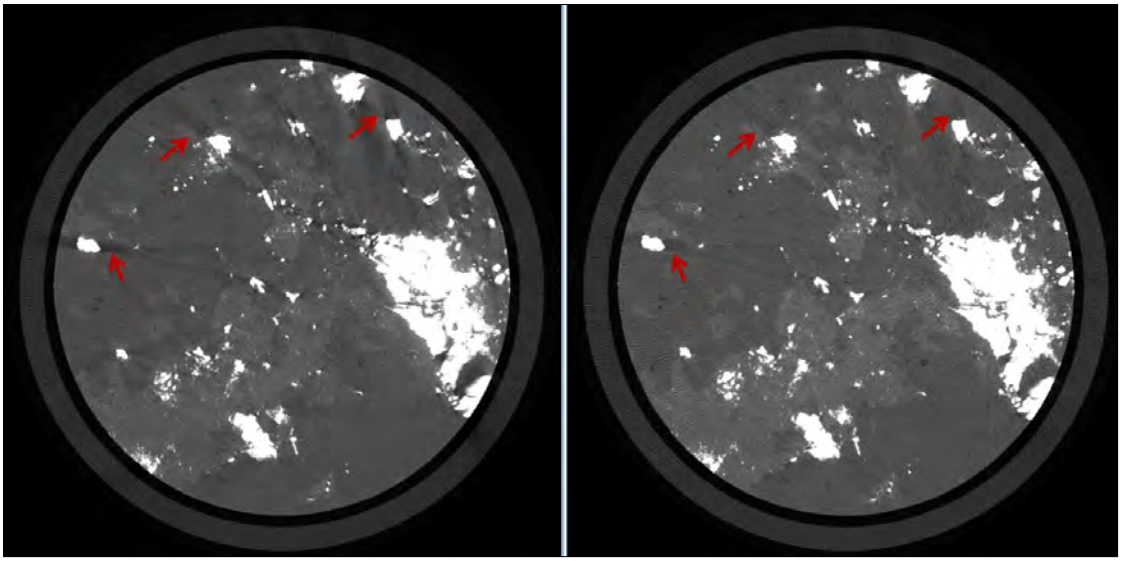

Figure 9: Scatter-Induced Artifacts in Reconstruction – ME-2 Core.
Left – without scatter correction. Right - with scatter correction.
In the uncorrected image, the arrows point to areas with scatter-induced streaks close to high-attenuation regions.
These streaks are greatly reduced in the scatter-corrected reconstruction.

Fig. 10 shows a profile plot taken through two small fractures and two different materials, in the scatter-corrected and traditional scans. We can see that it is difficult to differentiate between the fractures (red arrows) and the low-attenuation region (purple arrow) in the image reconstruction without scatter correction (Fig. 10, top left); the features appear with reduced contrast due to residual cupping artifacts. The profile plots show three regions with fairly similar attenuation coefficients (Fig. 10, bottom left).

By contrast, the scatter-corrected scan shows three distinct regions (Fig. 10, top right). Crucially, the contrast of the image is higher and the fractures have values with measured attenuation coefficients being close to 0 (Fig. 10, bottom right). This more accurately reflects reality, and is crucial for performing accurate image segmentation, estimation of porosity, and other DR analyses.

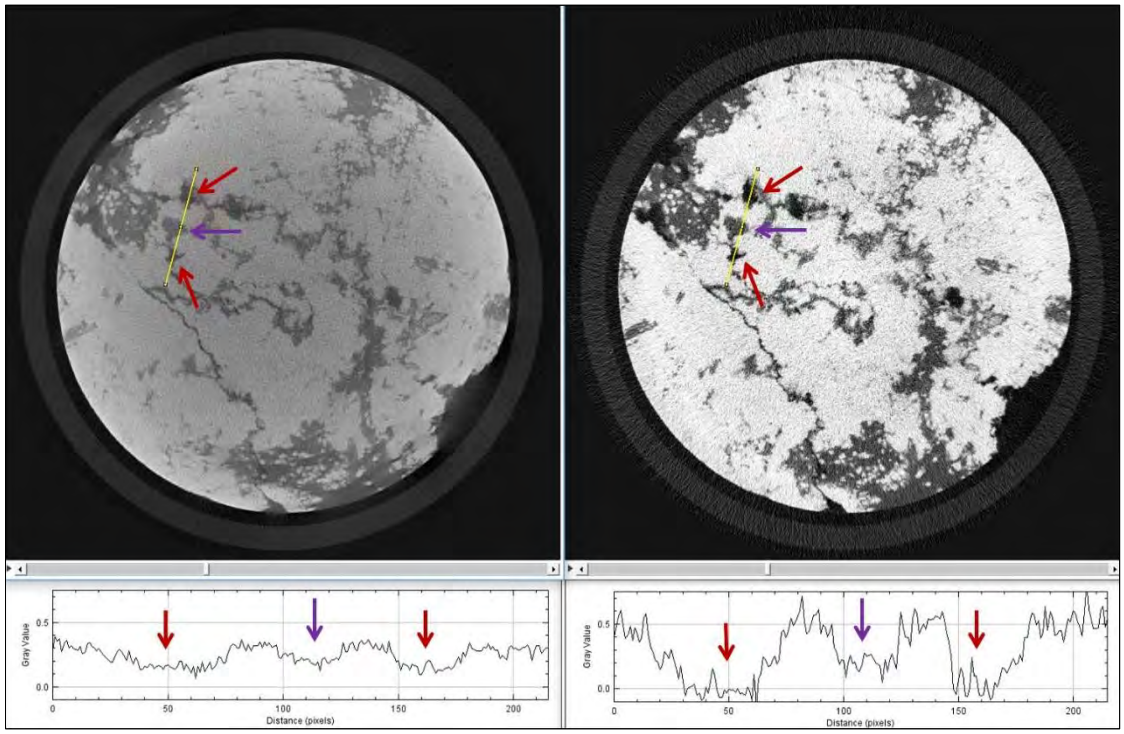

Figure 10: Cross-section of Reconstruction – ME-2 Core.
Left – without scatter correction. Right – with scatter correction.
Line plots are taken along the yellow lines in the images. The red arrows on the images and on the plots point to voids or fractures in the core, and the purple arrows point to a moderate-density portion of the core.
Note that the voids are centered around the true value of 0 in the scatter-corrected reconstruction (right line plot), while it is hard to tell the difference between the void and the moderate density portion without correction (left line plot).

Fig. 11 displays a cross-section taken through a highly-attenuating region of the core. Interestingly, over this slice of the core, the profile plot shows effects of residual cupping, which were partially corrected for in beam-hardening. Cupping is also a characteristic artifact of scatter (e.g., Schörner, 2012), and is especially visible in this region, where scatter was measured to contribute to more than 70% of the total signal experienced on the detector (see Fig. 5). Core ME-2 was observed to attenuate the most of any of the cores surveyed. This is partly due to on average higher material attenuation and partly due to the glass encasing used around the core. The high total attenuation greatly diminished the contribution of the primary component to the total signal and increased the scatter component, raising the scatter-to-total ratio to such a level.

Additionally, as in Fig. 10, several fractures are more easily distinguished from moderately-attenuating materials. The scatter-corrected reconstruction is noticeably noisier than the traditional scan's reconstruction. The scatter correction has revealed the true SNR of the primary signal by eliminating in some places upward of the 70% of the total signal that was scatter.

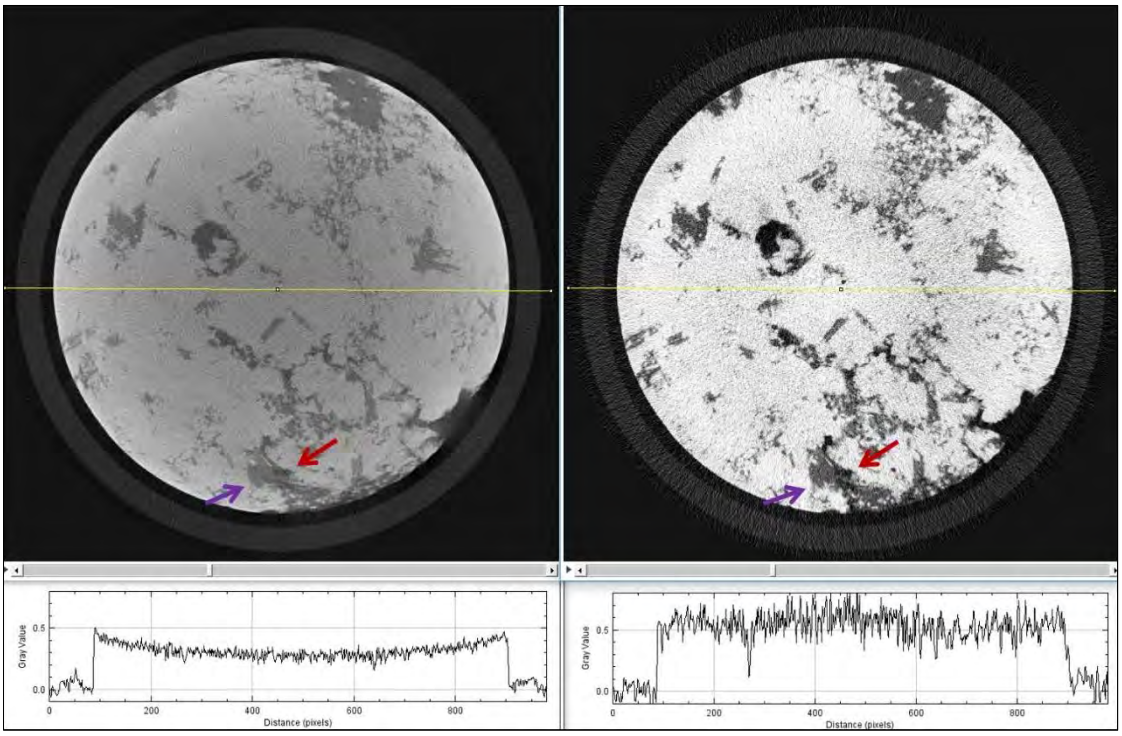

Figure 11: Cross-section of Reconstruction – ME-2 Core - Highly-Attenuating Slice.
Left – without scatter correction. Right – with scatter correction. Line plots are taken along the yellow lines in the images.
Red and purple arrows show regions of a fracture and a moderately-attenuating portion of the core, respectively. Difference between these two regions is better visible in the corrected reconstruction. The plots demonstrate that a heavy cupping artifact from scatter remains in the reconstruction without scatter correction, even though both reconstructions were corrected for beam-hardening.

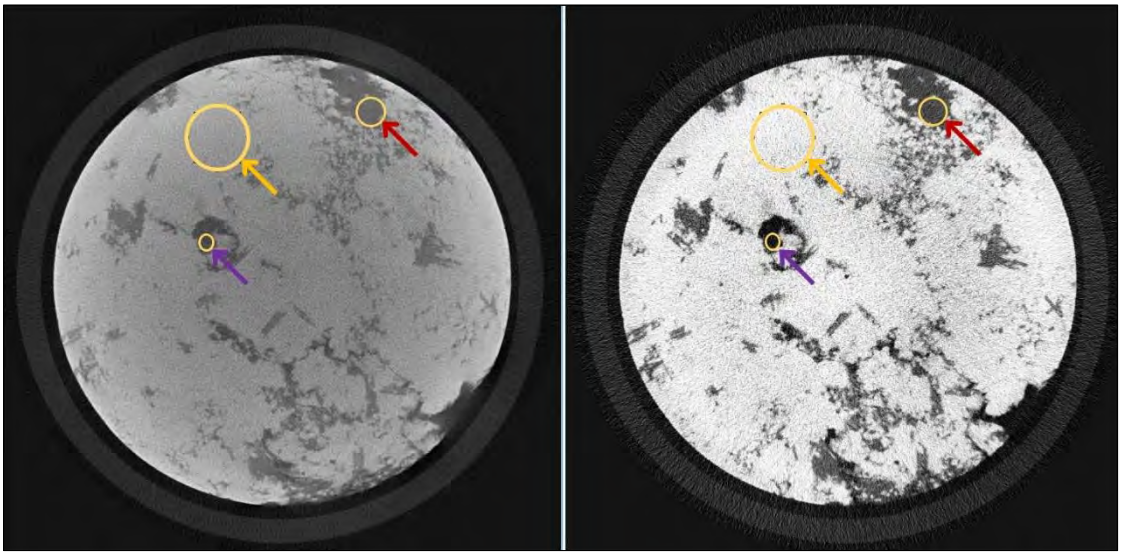

Figure 12: Cross Section of Reconstruction – ME-2 Core - Highly-Attenuating Slice, Numerical Values.
The regions inside orange circles were surveyed for quantitative evaluation of uncorrected (left) and scatter-corrected (right) reconstructions.
Regions surveyed: a void (purple arrow), moderately-attenuating material (red arrow), and highly-attenuating material (orange arrow).
In the void region (purple), the mean values reconstructed were 0.147 (uncorrected) and -0.006 (corrected).
In the moderately-attenuating region (red), the mean reconstructed values were 0.224 (uncorrected) and 0.145 (corrected).
In the highly-attenuating region (orange), the mean reconstructed values were 0.344 (uncorrected) and 0.580 (corrected).

Fig. 12 shows numerical results from both reconstructions. Three regions, of no-, moderate-, and high-attenuation, in the slice were surveyed and assessed for their mean values. In the non-attenuating (void) region, the mean values reconstructed were 0.147 (uncorrected) and ~0 (corrected). In the moderately-attenuating region, the mean reconstructed values were 0.224 (uncorrected) and 0.145 (corrected). In the highly-attenuating region, the mean reconstructed values were 0.344 (uncorrected) and 0.580 (corrected).

As stated above, Fig. 12 shows that the void region in the traditional scan had a mean attenuation coefficient of 0.147. This is of the same order as the moderately-attenuating material in Fig. 8. The residual cupping in this slice has significantly altered the observed values.

By contrast, the scatter-corrected reconstruction accurately reconstructs the void as having attenuation coefficient close to 0. The accuracy of the scatter-corrected reconstruction in a fracture gives credibility to its accuracy in other circumstances. A discrepancy in reconstructed values for non-air material was observed: values in the moderately-attenuating region differed by 35% between scans, and those in the highly-attenuating region by 40%. Given that the scatter-corrected scan is more accurate in the air, it is likely that the values in the traditional (air) uncorrected scan were underestimated in the highly-attenuating region.

Results for Core Sample ME-1

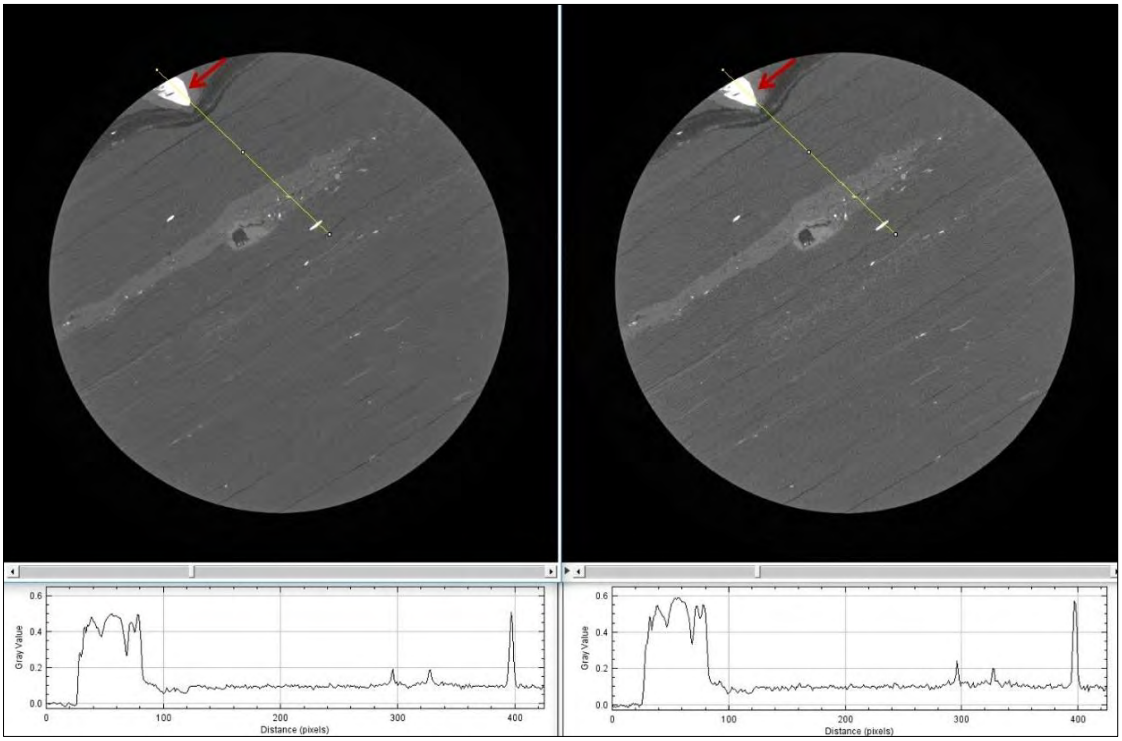

Figure 13: Cross Section of Reconstruction – ME-1 Core. Left – without scatter correction. Right – with scatter correction.
Note the difference in reconstructed values in the highly-attenuating regions (indicated by the red arrows).
This difference is not explained by differing BHC parameters, since both scans required the use of the same BHC parameter value.
See Fig. 14 for a visualization of the difference between the two images and more quantitative analysis.
Line plots are taken along the yellow lines in the images.

Fig. 13 shows a slice and profile plot taken across sample ME-1. On first glance, the slices on either side seem to be almost identical. There are no obvious artifacts from scatter in the scans. However, the profile plots reveal that the highly-attenuating region is observed to have different reconstructed values between both scans. This contrast is not as pronounced in the moderately-attenuating homogeneous region of the core.

Fig 14, which shows a voxel-wise subtraction of the reconstructions in Fig. 13, supports this observation. The highly-attenuating regions display the greatest difference between both scans, since they appear the lightest in the image. This difference is not explained by differing BHC parameters, since both scans required the use of the same BHC parameter value.

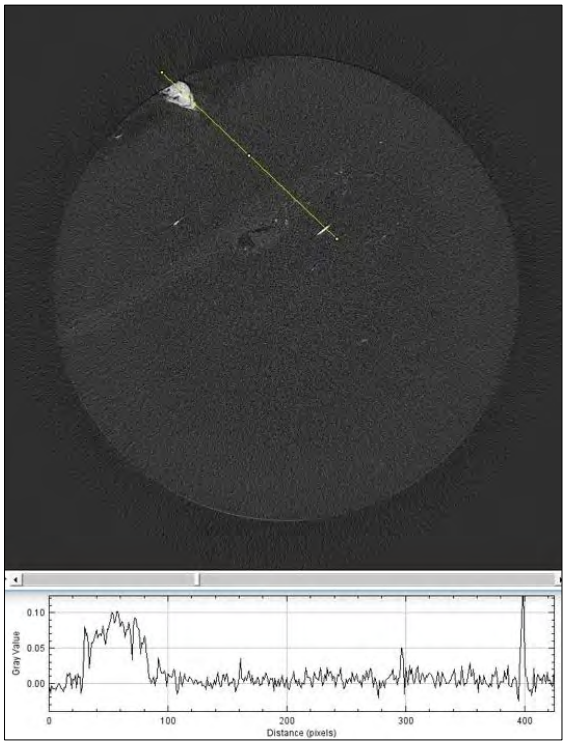

Figure 14: Difference of two reconstructions of ME-1 Core presented in Fig. 13.
This plot displays the difference between non-corrected (Fig. 13 left) and scatter-corrected (Fig. 13 right) reconstructions.
Note significant difference in reconstructed values in the highly-attenuating sections.
Line plot taken along the yellow line in the image.

Numerical results from three differently-attenuating regions of the ME-1 core were collected. These results are displayed in Fig. 15. The mean values reconstructed in the highly-attenuating region were 0.45 (uncorrected) and 0.53 (corrected). In the low-attenuation region values were observed to be 0.077 (uncorrected) and 0.077 (corrected). In the medium-attenuating region, values were 0.093 (uncorrected) and 0.098 (corrected).

These results confirm that the difference in the highly-attenuating region (~15%) far exceeds observed differences in reconstructed values in the moderately- (~5.1%) and low-attenuating (~0%) regions. Our experiments confirm the known fact (see, e.g., Schörner (2012) and references therein) that scatter artifacts reduce the apparent contrast of the reconstructed image. The highly-attenuating region is the most different from its surroundings of these three regions, and therefore is most affected by scatter. Medium- and low-attenuating regions are also affected, but to a lesser degree. The overall differences are distorted by the applied BHC.

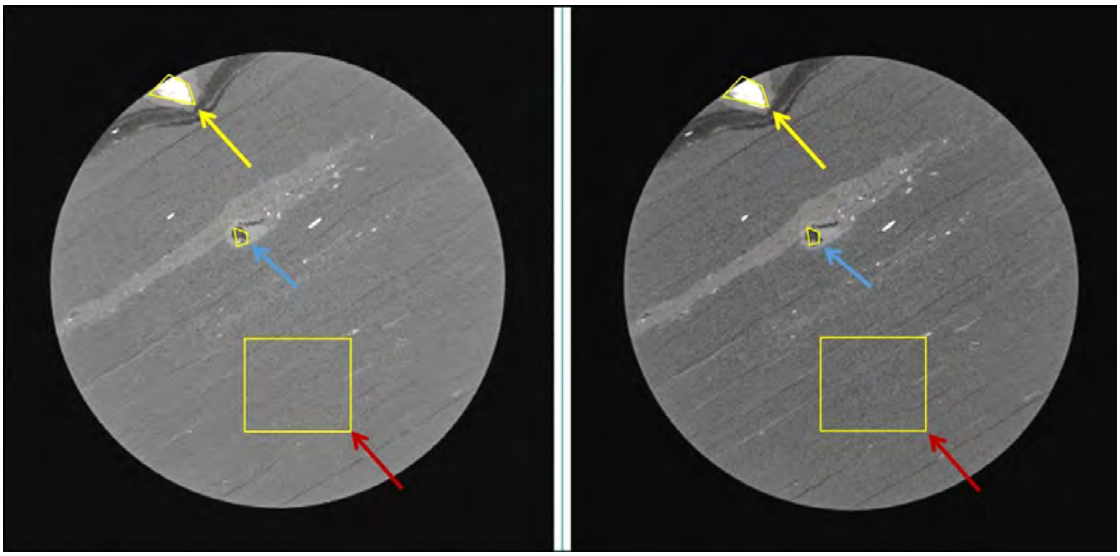

Figure 15: Evaluating Regions of Interest: ME-1 Core. Left – without scatter correction (uncorrected), right – with scatter correction. The mean values reconstructed in the highly-attenuating region (yellow arrows) were 0.45 (uncorrected) and 0.53 (corrected). In the low-attenuation region (blue arrow), values were observed to be 0.077 (uncorrected) and 0.077 (corrected). In the medium-attenuating region (red arrow), values were 0.093 (uncorrected) and 0.098 (corrected).

Results for Core Sample BEG-1

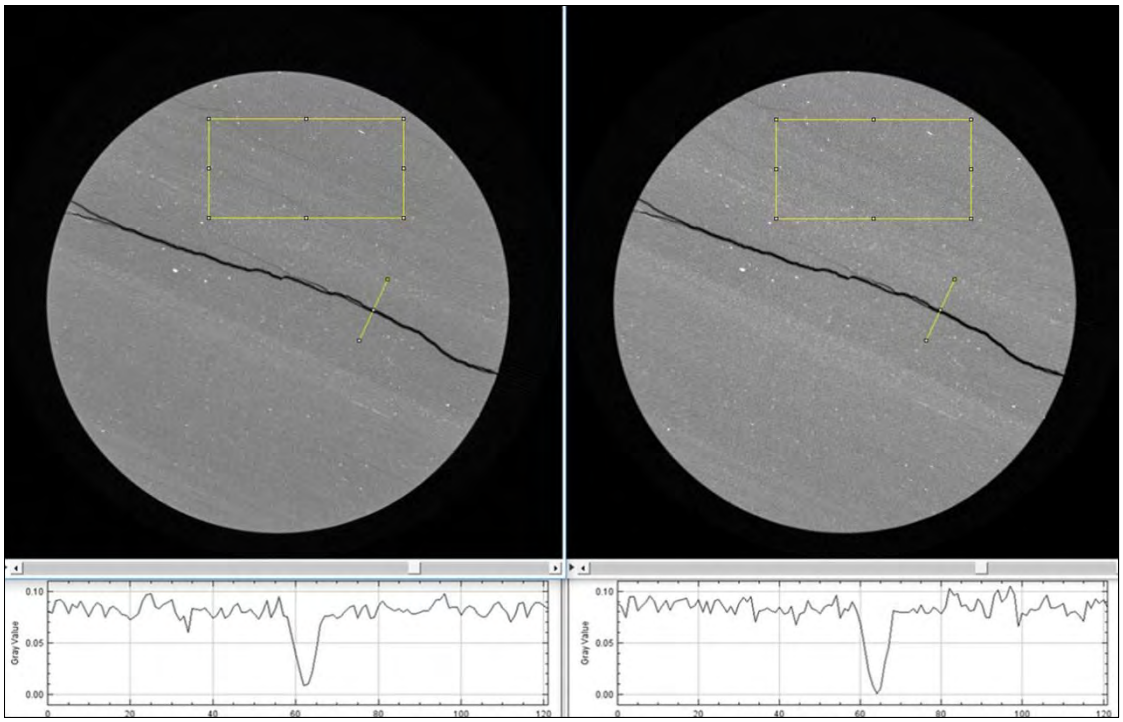

Figure 16: Cross Section of Reconstruction – BEG-1 Core. Left – without scatter correction. Right – with scatter correction. Mean reconstructed values inside of the yellow rectangle: 0.081 (uncorrected), 0.084 (corrected). Horizontal axis shows distance in pixels. Note the difference in reconstructed values, especially inside the air-filled fracture (e.g., see on line profiles at the distance ~63 pixels). The correct reading in the fracture should be 0 (as in the right image). Line plots are taken along the slanted yellow lines in the images.

In the BEG-1 scan as in the ME-1 scan, few scatter artifacts are visible upon first glance at the core. However, the attenuation plot along the line in Fig. 16Th (bottom left) clearly shows that the attenuation in the air-filled fracture is higher than the true value of 0 without scatter correction. This is a reconstruction artifact due to scatter that is corrected in the scatter-corrected scan (Fig. 16, right panel) and the attenuation in the fracture is now zero.

In addition, a survey of mean values in a homogeneous region of the core shows that there is a slight difference between the two reconstructions; this difference was measured to be 3.7%, with a value of 0.081 observed in the uncorrected for scatter image and 0.084 in the scatter-corrected image.

Results for Core Sample BEG-2

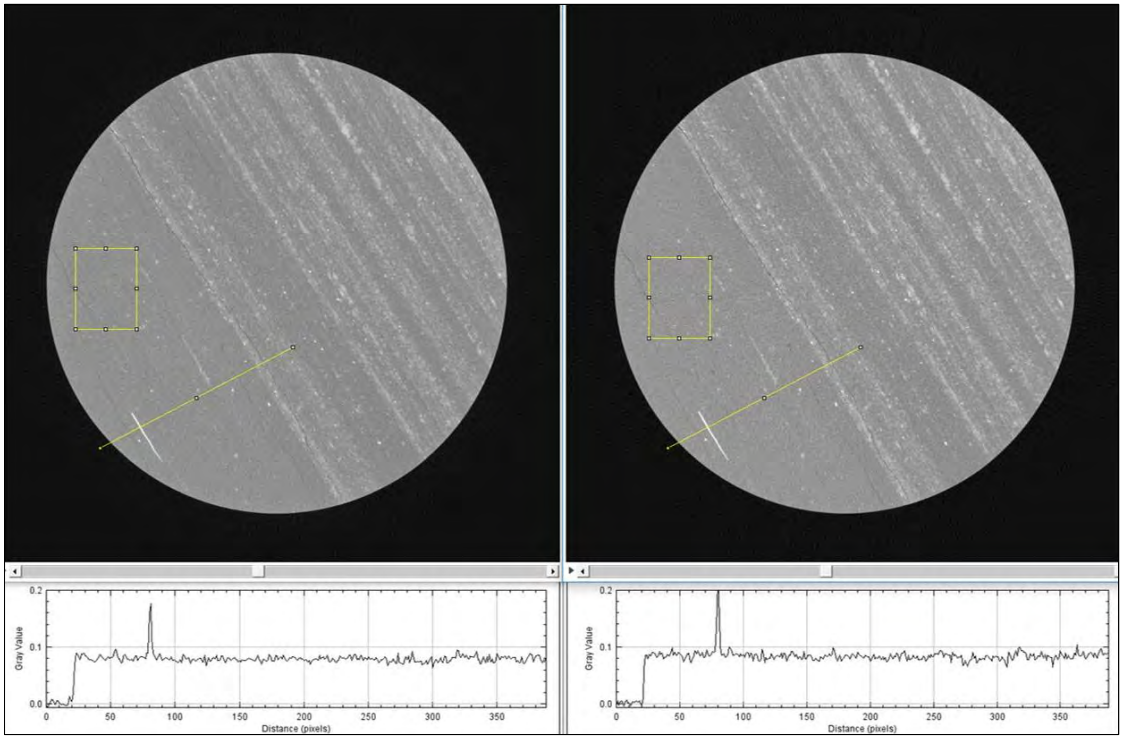

Figure 17: Cross Section of Reconstruction – BEG-2 Core. Left – without scatter correction. Right – with scatter correction. Mean reconstructed values inside of the yellow rectangle: 0.079 (uncorrected), 0.083 (corrected), which translates in to 5% difference. Note the difference in reconstructed values, especially at high attenuation regions (e.g., see on line profiles at the distance ~70 pixels). Line plots are taken along the slanted yellow lines in the images.

The reconstructions for core BEG-2 reveal similar information compared to the reconstructions performed for core ME-1.The reconstructed values over a homogeneous region of the core in the scatter-corrected (Fig. 17 right) and uncorrected (Fig. 17 left) reconstructed images are quite close, with mean values of 0.079 and 0.083 in the uncorrected and corrected scans, respectively. The difference is less than 5%. However, the higher-attenuating section in the bottom-left of the core has a greater apparent difference (~20%) in reconstructed values between the two images.

Discussion

Here general observations about scatter and its effect on image quality are compiled based on the results of this study.

1. The results demonstrate that scatter affects the reconstructed attenuation coefficients in heterogeneous samples (especially with higher attenuating cores) and cannot be ignored when high-quality quantitative analysis is required. Each of the four core scans presented highlight different ways that scatter impacts core image reconstructions in microCT. For example, results in the data domain (Fig. 7) show that more than 70% of the observed signal behind highly-attenuating regions of the ME-2 core is scatter. The reconstructions of the core demonstrate that without a proper correction, scatter leads to strong artifacts in these regions. Even in lower-attenuating core samples, reconstructions from scatter-corrected data produced more realistic and visually cleaner results compared to reconstructions from uncorrected data.
2. Generally, more dense cores lead to a higher scatter-to-total signal ratio. Also, the scatter signal produced by a core is sufficiently smooth and is not expected to vary as much as the attenuation of the core itself. Therefore, even locally, in the shadows of highly attenuating regions of the core, the scatter-to-total signal ratio can be dramatically increased.
3. Scatter removal reveals the true SNR. Since scatter signal is relatively smooth, subtracting it from the total signal may significantly increase the SNR, which is artificially low in an uncorrected scan. This effect may be most noticeable for highly attenuating cores, where, in some locations, scatter may constitute upward of 70% of the total signal. For example, the scatter-corrected reconstruction of the ME-2 core was noticeably noisier in the highly-attenuating regions than the traditional uncorrected reconstruction.
4. Scatter correction increases contrast, especially with small high-contrast inclusions. For example, contrast was drastically increased in the ME-2 scan. Regions of different materials, but with similar attenuation coefficient values in the uncorrected reconstructions, were much more easily resolved as being different in the scatter-corrected scan. This is explained by the fact that variation in the primary (exact) signal due to the variation of material properties of the core constitutes a greater percentage of the total observed signal, when the scatter component is removed. This is especially true of several small-size high-contrast inclusions surveyed in all four of the cores studied in this paper.
5. Scatter correction reduces streaks and cupping artifacts. These artifacts are well-known consequences of scatter in CT reconstruction. For example, streaking artifacts were observed a number of times in the ME-2 scan, near highly-attenuating regions in the reconstruction performed using uncorrected data. The BSA-based method for scatter correction was able to greatly reduce these artifacts in the corrected reconstruction.
6. Scatter correction provides more accurate attenuation coefficient values of the core image. From the reconstructions, it is apparent that the air-filled fractures in the uncorrected scans do not have correct attenuation values. In contrast, scatter correction consistently produces the correct attenuation coefficient of zero in these locations (see, e.g., Fig. 16, right panel). This key feature of the scatter-corrected scans is a strong indication that they are much more accurate. Additionally, streaking artifacts from highly-contrasting regions in the reconstructions from uncorrected data can negatively impact measured attenuation values in the regions where they occur.
7. Correcting data for scatter and improving image quality are important steps when performing material decomposition in significantly heterogeneous samples such as shales. Because a number of materials that compose shales have similar levels of attenuation, accurate recovery of material attenuation coefficient (μ) is critical. The comparison between the uncorrected and corrected reconstructions in Fig. 10, where low-attenuation regions become distinguishable from air-filled regions after scatter correction, is an example demonstrating the key benefit of these corrections.

In this work, we use two identical view samplings for the blank PMMA plate scan and BSA scan. Since scatter signal contains only low-spatial frequencies, it does not vary significantly between views. For this reason, the BSA scan is not required to be sampled in the view direction as finely as the blank plate scan. Scatter correction with a sparse BSA scan will be the subject of future work.

Conclusions

We showed that utilization of uncorrected for X-ray scatter core scan data leads to serious artifacts and inaccurate reconstructed attenuation coefficient values in microCT imaging. This is highly problematic when quantitative core

imaging, including determination of porosity, permeability, and bulk density, is the goal. MicroCT manufacturers, however, do not provide scatter correction solutions. This manuscript demonstrates a BSA method to directly measure and correct for scatter in microCT reconstructions of shale cores. Each of the four presented cases demonstrated significant positive impact of the proposed BSA-based X-ray scatter correction method on the accuracy of 3D core microCT imaging. The proposed BSA method is general and can be applied to different types of rock cores.

By directly measuring X-ray scatter, data correction can be implemented in the raw CT data domain without making assumptions about the size, mineral composition, and physical properties of the core being scanned. This approach is simple to implement and provides an accurate method for eliminating the detrimental effects of scatter on core image quality. Scatter correction is thus a key step toward accurate image reconstruction. In turn, the proposed BSA method will enable more precise multi-energy microCT and digital rock physics analyses of shales and other rocks.

Acknowledgements

The authors would like to thank Dr. Dan Georgi for his enthusiastic support of this project and valuable suggestions, Dr. Seongjin Yoon for his help in designing the BSA and scatter measurement experiments, and Gary Eppler for doing an excellent job in fabricating the BSA for the experiments. The authors express their gratitude to Aramco Services Company and iTomography Corporation for support and the permission to publish this paper.

List of Symbols and Acronyms

BSA	Beam-Stop Array.
PMMA	PolyMethyl MethAcrylate, also known as acrylic glass or Plexiglas.
BHC	Beam-Hardening Correction.
μ	Material attenuation coefficient.
$D_{a,i}$	The i-th view of the scan data taken with a blank PMMA plate between the core and source.
$D_{b,i}$	The i-th view of the scan data taken with the BSA between the core and source.
$D_{b,i}$	The scatter estimation data. Values behind each bead are interpolated to fill the whole frame.
G_a	The gain file, taken with the blank PMMA plate in front of the source and no core.
G_b	The gain file, taken with the BSA in front of the source and no core.
G_b	The scatter estimation data for gain files. Values behind each bead are interpolated to fill the whole frame.
P_i	The estimated primary signal without scatter; output of Equation (1).

References

Allison J., et al. (2016). Recent developments in GEANT4. Nuclear Instruments and Methods in Physics Research, 835 (1), 186–225, https://doi.org/10.1016/j.nima.2016.06.125.

Al-Owihan, H., Al-Wadi, M., Thakur, S., Behbehani, S., Al-Jabari, N., Dernaika, M., and Koronfol, S. (2014). Advanced Rock Characterization by Dual Energy CT Imaging: A Novel Method in Complex Reservoir Evaluation. In International Petroleum Technology Conference. International Petroleum Technology Conference.

Al-Sulami, G., Boudjatit, M., Al-Duhailan, M., and Simone, S. D. (2017). The Unconventional Shale Reservoirs of Jafurah Basin: An Integrated Petrophysical Evaluation Using Cores and Advanced Well Logs. In: SPE Middle East Oil & Gas Show and Conference. Society of Petroleum Engineers.

Almarzooq, A., AlGhamdi, T., Koronfol, S., Dernaika, M., and Walls, J. (2014). Shale gas characterization and property determination by digital rock physics. In: SPE Saudi Arabia Section Technical Symposium and Exhibition. Society of Petroleum Engineers.

Bootsma, G.J., Verhaegen, F., and Jaffray, D.A. (2013). Spatial frequency spectrum of the x-ray scatter distribution in CBCT projections. Med Phys., 40(11), 111901, https://doi.org/10.1118/1.4822484.

Coshell, L., Mclver, R. G., and Chang, R. (1994). X-ray computed tomography of Australian oil shales: non-destructive visualization and density determination. Fuel, 73 (8), 1317-1321.

GEANT4: Toolkit for the simulation of the passage of particles through matter - http://geant4.cern.ch/ [Accessed: March 25, 2018].

Gelb, J., Gu, A., Fong, T., Hunter, L., Lau, S. H., and Yun, W. (2011). A closer look at shale: Representative elementary volume analysis with laboratory 3D X-Ray computed microtomography and nanotomography. In International Symposium of the Society of Core Analysts (pp. 18-21).

Hakami, A., Al-Mubarak, A., Al-Ramadan, K., Kurison, C., and Leyva, I. (2016). Characterization of carbonate mudrocks of the Jurassic Tuwaiq Mountain Formation, Jafurah basin, Saudi Arabia: Implications for unconventional reservoir potential evaluation. Journal of Natural Gas Science and Engineering, 33, 1149-1168.

Lopez, O., Berg, C., Rennan, L., Digranes, G., Forest, T., Kristoffersen, A., and Boklepp, B. (2016). Quick Core Assessment from CT Imaging: from Petrophysical Properties to Log Evaluation. International Symposium of the Society of Core Analysts, Snomass, CO, paper SCA2016-031, pp 12.

Ly, C. V., Mintz, J., Bian, A., Andrew, M., and Bhattiprolu, S. (2017). Inter-Scaled Digital Core Analysis: From Core to Pore and Back. Unconventional Resources Technology Conference (URTeC).

NIST (2018): X-Ray Form Factor, Attenuation, and Scattering Tables Form Page. http://physics.nist.gov/PhysRefData/FFast/html/form.html. [Accessed: March 25, 2018].

Passey, Q. R., Bohacs, K., Esch, W. L., Klimentidis, R., and Sinha, S. (2010). From oil-prone source rock to gas-producing shale reservoir-geologic and petrophysical characterization of unconventional shale gas reservoirs. In: International oil and gas conference and exhibition in China. Society of Petroleum Engineers.

Poludniowski, G., Landry, G., DeBloir, F., Evans, P., and Verhaegen, F. (2009). SpekCalc: a program to calculate photon spectra from tungsten anode X-ray tubes, Physics in Medicine & Biology, 54 (19), N433, https://doi.org/10.1088/0031-9155/54/19/N01.

Sisniega, A., Zbijewski, W., Badal, A., Kyprianou, I., Stayman, J., Vaquero, J., and Siewerdsen, J.H. (2013). Monte-Carlo study of the effects of system geometry and antiscatter grids on cone-beam CT scatter distributions, Med. Phys., Vol. 40 (5), https://doi.org/10.1118/1.4801895.

Schörner, K. (2012). Development of methods for scatter artifact correction in industrial x-ray cone-beam Computed Tomography (Doctoral Dissertation, Technische Universität München).

Sossin, A., Rebuffel, V., Tabary, J., Létang, J. M., Freud, N., and Verger, L. (2016). A novel scatter separation method for multi-energy x-ray imaging. Physics in Medicine & Biology, 61 (12), 4711.

Suhrer, M., Cavanaugh, T., Diaz, E., Grader, A., and Joussaume, E. (2010, May). Imaging and Computing the Physical Properties of Gas Shale. In: Proceedings of the 2010 GeoCanada Conference - Working with the Earth (p.1-4).

Tiwari, P., Deo, M., Lin, C. L., and Miller, J. D. (2013). Characterization of oil shale pore structure before and after pyrolysis by using X-ray micro CT. Fuel, 107, 547-554.

Tenorio, O., E. (2016). A Comprehensive Study of the Eagle Ford Shale Fracture Conductivity, Texas A&M Univ.

Townsend, D. (2010). Imaging of structure and function with PET/CT. Molecular Imaging: Principles and Practice, Ralph Weissleder, Brian D. Ross, Alnawaz Rehemtulla, Sanjiv Sam Gambhir, People's Medical Publishing House–USA, Shelton, CT, 10-28.

Walls, J., and Armbruster, M. (2012). Shale reservoir evaluation improved by dual energy X-Ray CT imaging. Journal of Petroleum Technology, 64 (11), 28-32.

Wellington, S. L., and Vinegar, H. J. (1987). X-ray computerized tomography. Journal of Petroleum Technology, 39 (08), 885-898.

Wenk, H. R., and Bulakh, A. (2016). Physical properties. Minerals: their constitution and origin. Cambridge University Press.

Zhang, T., Ellis, G. S., Ruppel, S. C., Milliken, K., and Yang, R. (2012). Effect of organic-matter type and thermal maturity on methane adsorption in shale-gas systems. Organic geochemistry, 47, 120-131.

Zhang, T., Yang, R., Milliken, K. L., Ruppel, S. C., Pottorf, R. J., and Sun, X. (2014). Chemical and isotopic composition of gases released by crush methods from organic rich mudrocks. Organic Geochemistry, 73, 16-28.

Zhang, Y., Mostaghimi, P., Fogden, A., Middleton, J., Sheppard, A., and Armstrong, R. T. (2017). Local diffusion coefficient measurements in shale using dynamic micro-computed tomography. Fuel, 207, 312-322.